Technology and Health Care 13 (2005) 313–329
IOS Press

Reconstruction of human optic nerve heads for finite element modeling

Ian A. Sigal[a,b], John G. Flanagan[c,d], Inka Tertinegg[c] and C. Ross Ethier[a,b,c,*]
[a]*Department of Mechanical and Industrial Engineering, University of Toronto, Toronto, Canada*
[b]*Institute for Biomaterials and Biomedical Engineering, University of Toronto, Toronto, Canada*
[c]*Department of Ophthalmology and Vision Sciences, University of Toronto, Toronto, Canada*
[d]*School of Optometry, University of Waterloo, Waterloo, Canada*

Received 27 September 2004
Revised 24 December 2004

Abstract. *Purpose:* Glaucoma is a common ocular disease whose pathogenesis is hypothesized to involve biomechanical damage to optic nerve tissues. Here we describe a method for the construction of patient-specific models that can be used to evaluate the biomechanical environment within the optic nerve head. We validate the method using a virtual eye, and demonstrate its use in computing optic nerve head biomechanics.

Methods: Human eyes were imaged and the optic nerve head region was processed to allow serial plastic histologic sections to be cut. These sections were photographed, unwarped and aligned so as to reconstruct three-dimensional patient-specific models incorporating sclera, pre- and post-laminar nerve, lamina cribrosa, and pia mater. Deformations, stresses and strains were computed in the resulting model using finite element techniques.

Results: The approach successfully reconstructed patient-specific optic nerve head models. Reconstruction of a virtual eye showed excellent agreement between the true and reconstructed geometries, and between the deformations and strains computed on the true and reconstructed geometries. A sample reconstruction showed reasonable agreement between computed and measured retinal surface deformations.

Conclusion: The technique presented here is viable and can be used to accurately compute human optic nerve head biomechanics.

Keywords: Glaucoma, optic nerve head, IOP, biomechanics, finite elements, stress, strain

1. Introduction

Glaucoma is a leading causes of blindness, with 65–70 million people suffering from the disease world-wide [1]. Loss of vision in glaucoma is due to damage to retinal ganglion cell axons, responsible for transmitting information from the retina to the visual centres in the brain. Evidence shows [2] that axonal damage occurs at the level of the lamina cribrosa (LC), a specialized structure in the optic nerve head (ONH) in the posterior eye (Fig. 1).

The pathogenesis of glaucoma remains unclear and controversial [3]. The eye is internally pressurized, with a normal intraocular pressure (IOP) of 15 mmHg. Elevated IOP is the principal risk factor for the

*Address for correspondence: C. Ross Ethier, Department of Mechanical and Industrial Engineering, 5 King's College Road, University of Toronto, Toronto, Ontario M5S 3G8, Canada. Tel./Fax: +1 416 978 6728/-7753; E-mail: ethier@mie.utoronto.ca.

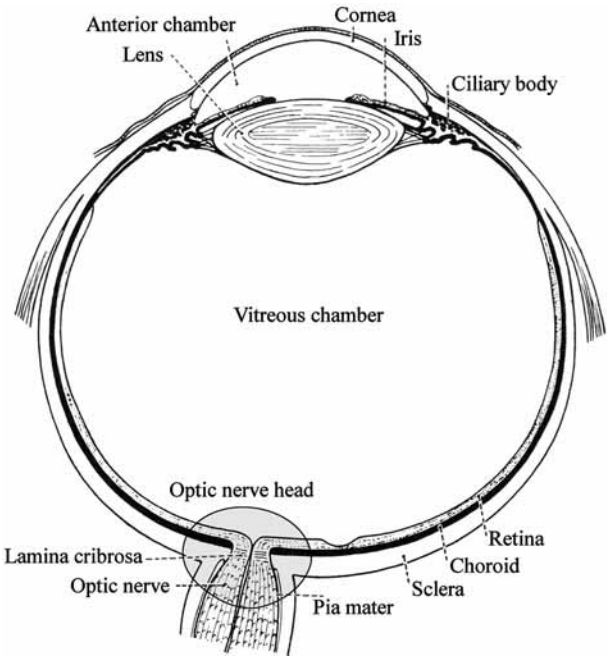

Fig. 1. Cross section through a human eye. The vitreous chamber is filled with the vitreous humor, which exerts a pressure on the surface of the retina (the pre-laminar neural tissue). Visual information is transmitted to the brain by retinal nerve fibres that converge at the back of the eye to form the optic nerve, exiting the eye through the scleral canal in the optic nerve head region. The lamina cribrosa acts as a connective tissue support that spans the scleral canal. Adapted from [32, p. 2].

development of glaucoma [4–6], yet the mechanism(s) by which elevated IOP contribute to glaucomatous optic neuropathy remain unclear. For example, not all people are equally susceptible to elevated IOP: some people suffer glaucomatous damage at an IOP of 15 mmHg, while others remain apparently unaffected by pressures of 30 mmHg or more. A better understanding of the mechanisms of axonal damage and the sources of the differences in susceptibility to elevated IOP is needed.

The mechanical damage theory of glaucoma hypothesizes that retinal ganglion cell damage in glaucoma is the result of IOP-induced strain and stress within the lamina cribrosa that can reach pathologic levels [7–9]. It is suggested that differences in the anatomy and composition of the ONH tissues between individuals leads to different susceptibilities to elevated IOP. To evaluate this possibility a characterization of the biomechanical environment within and around the optic nerve head is needed, accounting for inter-individual differences in ONH anatomy.

The relative inaccessibility of the ONH has made direct experimentation difficult, and although some valuable information has been obtained from experiments [10,11], they do not provide a detailed picture of the biomechanical environment within the ONH. Simplified biomathematical models of the optic nerve head have also been developed [12–14]; although valuable, they have lacked the necessary detail to accurately model biomechanical behaviour. More complex geometries have been studied by computational methods. Modeling the LC and immediate peripapillary sclera Bellezza et al. [15] found that LC eccentricity had a significant effect on the stress distribution within load-bearing tissues of the ONH. However their models still assumed constant laminar thickness and, like the biomathematical models, a uniform IOP acting directly on the anterior LC surface. The IOP acts on the vitreo-retinal interface, not directly on the LC, and forces on the LC can be different and even have a tangential component.

In [16] we considered ONH biomechanics in greater detail. Our models were axisymmetric but included the lamina cribrosa, the peripapillary sclera, the pre-laminar and post-laminar neural tissues, and the pia mater. They also allowed for more realistic boundary conditions. A preliminary geometric sensitivity analysis and a parametric study of the effects of material properties revealed that strain and stress levels within the lamina cribrosa depend strongly on scleral properties.

In this work we take modeling of ONH biomechanics one step further, by introducing a method to construct individual-specific models of human optic nerve heads from histomorphometric data. These models will serve as the foundation for an investigation into the etiology of glaucoma and the sources of the differences in susceptibility to elevated IOP between individuals. We describe the model construction method and illustrate the steps with a sample reconstruction of an individual-specific ONH. We then show how this model can be used in finite element calculations of optic nerve head biomechanics. We also evaluate the quality of the construction method by applying it to a virtual eye with known geometry.

2. Methods

Our goal was to produce a model that was computationally tractable and that maintained good fidelity to the original tissue architecture. The model construction method consisted of the following major steps: eye preparation, optic nerve head sectioning, imaging, image alignment, segmentation, interpolation, surface and volume meshing and finite element pre-processing (including setting boundary conditions). Below is a description of each step.

2.1. Eye preparation

Ostensibly healthy eyes were obtained within 24 hours post mortem from the Eye Bank of Canada and prepared as previously described [10,17,18]. Eyes were obtained and managed in accordance with the provisions of the Declaration of Helsinki for research involving human tissue. To prevent blood efflux the optic nerve was tied off 3 mm from the ONH. Since the eyes had been used for corneal donation, the sclera was cut at the level of the pars plana and the iris and lens were removed. Lenticular remains and the majority of the vitreous were then removed by vitrectomy. A fluid seal around the periphery of the incision was provided by a modified apparatus, consisting of a collar incorporating two cannulae and a lens that was glued to the sclera with cyanoacrylate adhesive. This procedure replaced the possibly opaque lens in the post mortem eye with high-quality optics, permitting excellent quality images of the ONH, while allowing rapid infusion of fixative through the cannulae. It also protected the posterior half of the eye from mechanical stress and prevented retinal detachment. Figure 2 shows a photograph of an eye being prepared for an experiment.

The eye was placed in a custom chamber filled with physiological saline that mounted to the vertical rails of a standard slit-lamp headrest. Eye temperature was maintained at 37° by thermostatic control of chamber saline temperature. In some experiments, the chamber pressure was 3.5 mmHg to represent cerebrospinal fluid pressure at eye level. By adjusting the level of saline in a reservoir connected to one of the cannula, while the other was clamped off, IOP was sequentially set to 5, 15, 22, 30, 40 and 50 mmHg above chamber pressure. At each pressure, after the eye was allowed to equilibrate for 15 minutes to allow for viscoelastic relaxation (see below), seven topographic image series were acquired with a scanning laser tomographer (Heidelberg Retinal Tomograph, Version 2.01a, Heidelberg Engineering, Germany). Each series consisted of 32 images with a 10° field of view centered on the ONH scanned at 256×256 pixels resolution. IOP was then set to either 5 or 50 mmHg above chamber pressure, and

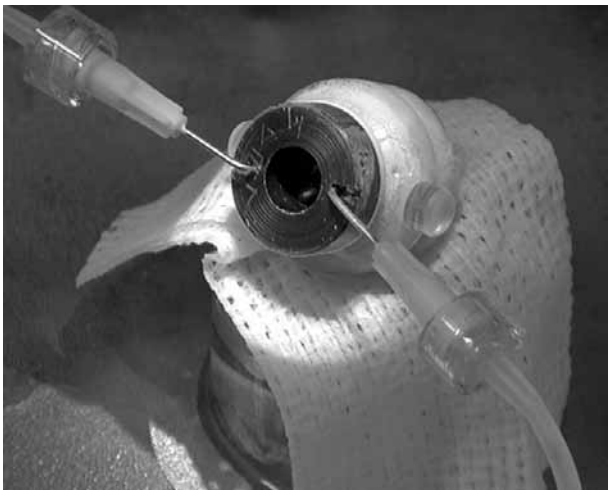

Fig. 2. Photograph of a human eye during preparation for an experiment. The anterior portion of the eye has been replaced by a collar containing two cannulae and a lens. The cannulae allow control of the intraocular pressure (IOP) as well as rapid infusion of fixative. A scanning laser tomographer (HRT) images the topography of the retina through the lens.

after equilibration, the eyes were scanned with the Heidelberg Retinal Tomograph (HRT) and perfusion fixed by rapidly exchanging the isotonic saline with 2.5% paraformaldehyde/2.5% glutaraldehyde in Sorenson's phosphate buffer and maintaining IOP for 24 hours.

Optic nerve head tissues exhibit viscoelastic behaviour [7,19]. Since elevated levels of IOP are present for months or years in glaucoma, we were not interested in the short-term (transient) response of the tissue to pressure. Instead, our modeling concentrated only on the elastic component of the tissue's behaviour, and in the experimental studies it was therefore important that eyes be mechanically equilibrated after a pressure change. In a small study involving a subset of eyes we therefore studied the time course of equilibration by taking HRT images of retinal topography every five minutes for half an hour after IOP changed.

2.2. Optic nerve head histology and imaging

After fixation, the ONH and surrounding sclera were excised, dehydrated in a graded series of ethanols, and placed into an embedding mould. Sutures made of collagen strands derived from mammalian gut, 70 to 100 μm in diameter (6–0 gut sutures) were placed into the mould using a custom jig that allowed the sutures to be kept under tension and pass straight across the mould at known positions and serve as fiducial markers (Fig. 3). The ONH and fiducials were then infiltrated with JB-4 plastic. After curing, sagittal serial sections 2 μm thick were cut across the entire ONH, at right angles to the axes of the fiducial markers. Sections at intervals of approximately 100 μm were selected for subsequent staining and imaging. The selected sections (typically 18–21 per ONH) were digitally photographed under dark field illumination (Leica MZ6, Heerbrugg, Switzerland) using a Nikon Coolpix 990 digital camera (2048 $\times$ 1536 pixels, 8 RGB bits per channel per pixel) and saved in TIFF format. Special attention was paid to lighting and photographic conditions so that images were uniformly illuminated and the sclera was unsaturated on an 8-bit grey scale. The sections were then stained with picrisirius red to identify collagen and solochrome cyanine to identify myelin, nuclei and blood cells. The dual-stained sections were then digitally photographed under bright field illumination using the same procedure, and the digital images

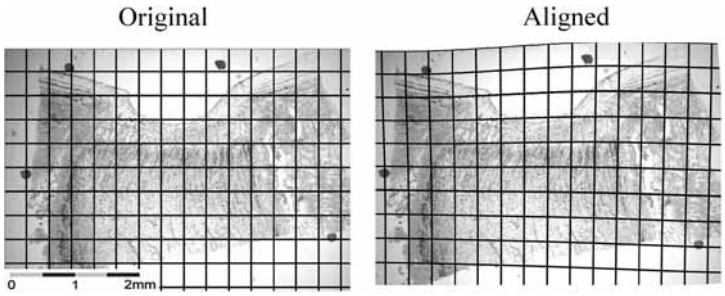

Fig. 3. Digital photographs of tissue sections are aligned to form a stack, using fiducial markers inserted before the sectioning (see text for details). The left panel shows a typical sagittal cross section (bright field photograph, dual stained with contrast digitally enhanced) with a superposed grid. The fiducial markers are the four dark dots. The right panel shows the same section after forced non-rigid alignment to a reference image of an undeformed sample. These photographs were converted from color to greyscale for publication.

were inspected for quality control. Some sections were unusable (for example, due to tissue damage or deformation), and an adjacent section was used, typically within 4–6 μm of the original section.

The amount of shrinkage was estimated from comparison between the HRT images and the reconstructions. The shrinkage was variable but did not exceed 3.5%, and in fact was frequently less than the uncertainty in the alignment of the HRT images and the reconstructed tissue sample.

Stained sections do not always have consistent stain penetration (for example due to variations in section thickness), which results in some sections appearing darker than others. This could lead to artefacts during segmentation, and we therefore applied automated grey-level normalization using Photoshop (Adobe Systems Inc, USA) to the image "stack".

2.3. Image alignment

Images were aligned based on the fiducial positions, defined as the location of the centroid of the fiducial cross-section. The centroids were easy to locate visually as the fiducials generally retained their initial circular cross-section. The centroid locations were marked on each image, and a transformation to return these to their known reference locations was applied. This transformation included rotation, translation and unwarping to compensate for deformations caused during sectioning and mounting . The unwarping process assumed that the sections were thin elastic sheets and that the deformations were small, and used a custom modified version of TPSSuper (F. James Rohlf, SUNY, Stony Brook, NY), which allowed alignment of a whole stack of images to one reference image (Fig. 3). The reference image was a photograph of the uncut block. The root mean square variability in the position of the fiducial marker between slices was approximately 15 μm.

The above approach has an advantage over using anatomical features as landmarks, which can lead to "straightening", where some structures that should not align section-to-section are matched [20]. The final magnification of images was determined by using measurements of inter-fiducial distances in the uncut block.

2.4. Segmentation

Tissue regions were manually highlighted and labelled (segmented) using Amira 3.1 (TGS Inc, France) on each histologic section (Fig. 4). We segmented five different tissues: sclera, pre-laminar neural tissue (including retina), lamina cribrosa, post-laminar neural tissue (including optic nerve) and pia mater.

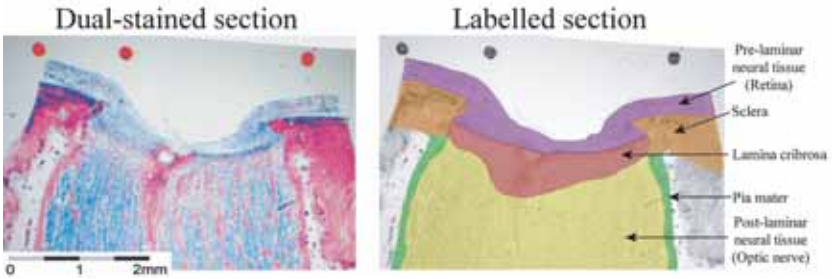

Fig. 4. The left panel shows a typical sagittal cross section of dual-stained tissue photographed under bright field conditions. The right panel shows the same section after segmentation. Five different tissue regions are defined. Superior side is right.

Segmentation used a combination of dark and bright field images of dual-stained sections. A manual approach proved to be more robust than an automated one, and gave models that better matched the original histologic sections.

We began the segmentation process by identifying the sclera from both dual-stained and dark-field images. The intensity of the picrisirius staining and the density and organisation of the tissue in the darkfield image determined the classification. Sclera was dense and fibrous in the dark-field images and in the stained images had the most intense staining. The pia mater was bright and amorphous in the dark-field and also stained well for collagen, albeit less than the sclera. The vitreo-retinal interface was clearly distinguishable in the double-stained sections. The anterior surface of the lamina cribrosa was defined by the termination of the radial laminar beams and the insertion points at the sclera, while the posterior surface was defined by two attributes: The first was the termination of solochrome cyanin staining, indicating a lack of myelination inside the lamina cribrosa [8]. The second was that the connective tissue beams showed the "stacked plate" morphology typical of the lamina cribrosa [21,22]. This was most easily seen in dark field images. The segmentation of the lamina cribrosa also completed those of the pre- and post-laminar neural tissues.

Some eyes developed detached retinas during histologic processing. Since these did not represent the *in vivo* or even experimental situations, we manually translated and rotated the detached regions of the retina until they were again in contact with the anterior surface of the sclera.

Between each original section pair we inserted two evenly spaced cubic interpolated sections, reducing inter-section distance from ~ 100 μm to ~ 33 μm. Interpolation sometimes introduced artefacts, for example, an interpolation of two smooth pia mater segmentations could produce a sharp edge and/or an optic nerve exposed to the exterior. These were manually cleaned and smoothed.

2.5. 3D reconstruction and surface meshing

Amira was used to generate a triangulated surface mesh enclosing the segmented tissue regions using a generalized marching cubes algorithm. This approach had both advantages and disadvantages [23–25]. The advantages were that the surfaces were closed and fully enclosed each tissue region; that the surface mesh could be verified to be topologically correct (no self intersections, badly oriented triangles and/or badly shaped elements, as measured by aspect ratio or internal angles); and that the different tissue regions defined by the segmentation were always separated by a surface. The major disadvantage was that a set of 2D segments do not define a unique 3D surface, and sometimes the surface triangulation led to "islands" (one tissue region inside another) and "holes" (e.g. an opening in the pia mater so that the optic nerve was exposed to the subdural space). Therefore, the segmentation and surface meshing

were an iterative process, where we generated a surface mesh, evaluated its quality and refined the segmentation to improve the outcome, typically with small adjustments and editing of the interpolated sections. For example, to better guide the surfacing algorithm to produce a continuous pia mater sheath around the optic nerve, we slightly increased the pia mater segmented thickness. Jumps ("ridges") on surfaces could usually be reduced by small manual adjustments (usually of a few μm) in the relative alignment of adjacent sections. This was generally most evident in the vitreo-retinal interface, where a smooth reconstructed surface was expected, and in the scleral canal, where a smooth oval-shape was expected.

Surface meshes were extremely detailed, containing 2–5 million elements (1–2 million nodes), depending on the smoothness of the segmentation. This would result in a 3D volume mesh that would be too large for finite element calculations with current computational resources, and therefore the surface mesh was downsampled using Amira's automated simplification modules to about 30,000 surface elements ($\sim$ 14,000 nodes) in several stages. This gave a reasonable trade-off between accurate tissue boundary definition and computational resources (Section 2.10). The downsampling was done in such a way as to remove all highly elongated elements (95% of the final surface elements had an aspect ratio lower than 6), and very small or very large elements (95% of the final surface elements had mean edge lengths of 80 ± 30 μm).

2.6. Reconstruction quality assessment

To assess the quality of the reconstruction we registered the optic disk topography obtained with the HRT before eye fixation with the reconstructed vitreo-retinal interface. This was done in Amira first by manual translation, rotation and scaling, until a good match was observed. The root mean square (rms) of the distance between closest nodes from each vitreo-retinal surface was used as measure of inter-surface distance [26]. The automated registration algorithms were then used until a relative rms $<$ 0.0001 was achieved. Since retinal detachment was not observed in the HRT image, only regions with no retinal detachment were considered in the reconstructed vitreo-retinal interface registered.

The registration transformation was then applied to a reconstruction of the major retinal blood vessels on the histological sections that were clearly identifiable in the dual stained sections. The vascular tree was then superposed on the HRT images to verify that the resulting geometry matched that seen in the HRT reflectivity image.

2.7. Volume meshing

To compute ONH deformations using the finite element method, a volume mesh was required. This mesh was generated in Amira from the surface mesh using the advancing front technique [26]. This method generally creates good tetrahedra near the boundaries, but is less effective inside the domain [27] and requires as source a surface mesh that is topologically correct, with no intersected or badly oriented elements. This sometimes required small alterations to the segmentation to improve the corresponding surface mesh.

A typical volume mesh consisted of 33,000 nodes, forming 30,000 tri-node surface shell elements (SHELL63 in ANSYS) and 170,000 four-node tetrahedral volume elements (SOLID45), with 95,000 degrees of freedom (DOF). The meshes were then ported from Amira to the finite element software (ANSYS v6.1) using a custom macro in Ultraedit 10 (IDM Computer Solutions Inc., Ohio USA). In ANSYS the shell elements were used to define node sets (components), for later application of boundary conditions, and deleted.

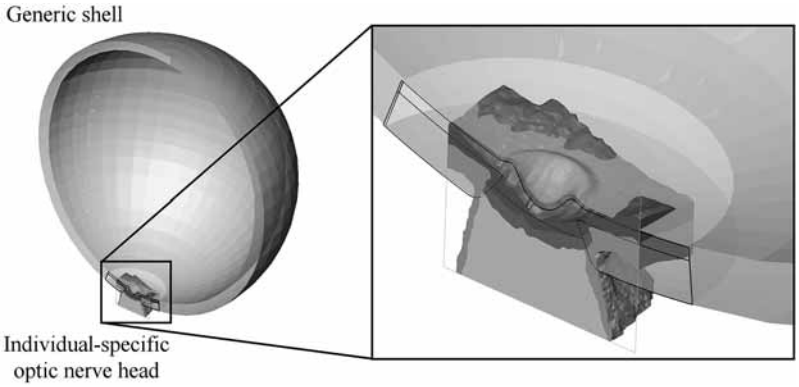

Fig. 5. Example of the "embedding" of an individual-specific optic nerve head model into a generic spherical shell for application of boundary conditions. The models have been cut through the middle, with the generic shell model shown semi-transparent for clarity. On the left is an overview, and on the right a detailed view of the optic nerve head region. The deformations computed for the generic shell are then enforced on the sides of the individual-specific models.

2.8. Finite element modeling

Material properties were assigned as previously reported [16]. All tissues were assumed to be homogeneous, practically incompressible ($v = 0.49$), and linearly elastic. Young's modulus values were obtained from the literature where available (sclera: 3 MPa; neural tissue: 30 kPa), or were estimated based on indirect measurements in the literature (LC: 300 kPa; pia mater: 3 MPa).

Only the optic nerve head region was reconstructed for individual-specific modeling, but in actuality the optic nerve head region is mechanically coupled to the rest of the ocular shell. We therefore "embedded" the individual-specific optic nerve head model into a generic spherical shell that incorporated a generic ONH that was an axially rotated version of the models previously described [16], and is the same used for the virtual eye model described in Section 2.9. First, the IOP-induced deformations of the generic shell were computed in a pre-processing step. The generic shell model contained approximately 665,000 nodes forming 468,000 ten-node tetrahedral elements (SOLID92) with 2 million DOF. Second, the individual-specific optic nerve head model was fit to the optic nerve head region of the generic shell by manual rotation and translation in Amira (Fig. 5). This allowed the location of the side boundary nodes on the individual-specific model to be mapped to positions within the generic shell. It was not possible to perfectly match the individual-specific model to the generic shell, so we concentrated on matching the sclera, since previous computations [16] suggest that scleral mechanics have an important role in determining optic nerve head deformations, while the relatively compliant pre-laminar neural tissue (retina) has a much more limited effect. Finally, computed deformations from the generic shell were mapped to side boundary nodes on the individual-specific optic nerve head model. The entire set of boundary conditions for the individual-specific model therefore consisted of: (1) these specified side surface displacements; (2) an intraocular pressure applied to the vitreo-retinal interface of the individual-specific optic nerve head; and (3) zero pressure on the external surfaces of the individual-specific optic nerve head, including the cutting surface of the optic nerve.

Solutions were computed using the PCG solver with default parameters, and typically required less than 30 minutes of CPU time on a desktop workstation with Windows XP SP1, an AMD Athlon XP 2100+ CPU and 1.5 GB of memory (1.25 GB total ANSYS workspace/500 MB database).

2.9. Quality control using a virtual eye

To test the accuracy of our model construction technique, a digital model of an idealized 3D eye (a virtual eye) was constructed and segmented. The virtual eye was generated by rotating the 2D Model 1 described in [16] around its axis of symmetry, retaining the geometry and material properties of each tissue region. Briefly, the virtual eye consisted of two concentric spherical shells: an exterior sclera/cornea 0.78 mm thick, and an interior retina 0.24 mm thick that tapered away to zero thickness at 120° anteriorly from the ONH. The ONH incorporated an optic cup and a scleral canal. The LC was 0.3 mm thick with an anterior surface diameter of 1.8 mm. This is the same 3D model used for boundary conditions. The material properties assigned were the same as for the individual-specific models, described in Section 2.8.

Virtual sections at 33 μm intervals through the ONH of the virtual eye were generated and used to reconstruct an ONH model using the techniques described above. Predictions of the mechanical response to IOP were computed using the finite element method using the same method as for individual-specific models.

2.10. Mesh refinement studies

We carried out a mesh refinement study, evaluating mesh-independence by monitoring two aspects of the solution when IOP changed from 5 to 50 mmHg: the predicted vitreo-retinal deformation field, and the corresponding maximum principal strain field. When refinement of a model failed to produce a significant change in these quantities we considered the model sufficiently resolved. We defined a "significant change" in a computed quantity to be one that would alter the conclusions we derived from the analysis of the model.

Two different mesh refinement strategies were available. Models could be ported into ANSYS and refined using ANSYS's own tetrahedral refinement algorithms. Alternatively models could be generated with varying mesh resolutions in Amira before being ported into ANSYS. With the first method it is possible to use adaptive refinement routines within ANSYS and hence minimize computational cost. However, this would require downsampling the model geometry in Amira before porting it to ANSYS, which negatively affects the reconstructed geometry. Since our main goal was to accurately reproduce the geometry of individual-specific ONHs, we opted for the second method.

Four-node tetrahedral elements are generally not recommended for solid deformation modeling [28, 29]. Therefore after importing a model into ANSYS the 4-node tetrahedrals (SOLID45 in ANSYS) were converted into more accurate 10-node tetrahedrals (SOLID92) and mid-side nodes added to all sides. For example, after modification of a 170,000 element mesh, the number of nodes increased from 33,000 to 250,000 (DOF increase from 95,000 to 740,000).

3. Results

3.1. Reconstruction and computations using a virtual eye

A comparison of the 3D reconstructed model geometry and the original (true) virtual eye ONH geometry is shown in Fig. 6. The reconstructed model is formed by approximately 46,000 nodes and 273,000 4-node tetrahedral elements. Some small differences between the models are visible; for example, edges of the elements used to create the surfaces in the reconstructed model can be seen along

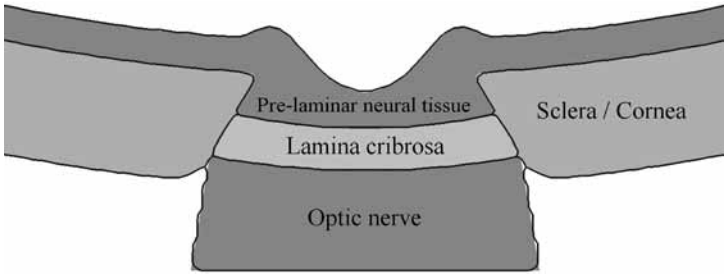

Fig. 6. Comparison of cross sections of original 3D virtual eye optic nerve head (shaded regions) and 3D reconstructed model outline (dark lines). Very good agreement between the original and reconstructed geometries is evident.

the sides of the optic nerve. Also, sharp corners in the original model have been slightly changed (see the sides of the lamina cribrosa, the tips of the sclera and the posterior optic nerve.). There is also now a small interface between the optic nerve and the sclera. However, the overall agreement is very good, and the differences represent small fractions of the total region volumes. For example, the total volume of the reconstructed geometry is within 0.2% of the original. This indicates that the reconstruction process produced a faithful replica of the virtual ONH.

The effects of mesh refinement and element type on predicted displacement and maximum principal strain fields were investigated in two series of meshes derived from the model shown in Fig. 6. In one series the elements were refined and kept as 4-node tetrahedra, in the other the elements were first converted to 10-node tetrahedra and then refined. To keep model geometry constant, refinement was done using ANSYS internal algorithms [28]. Mesh resolutions ranged from approximately 46,000 nodes and 273,000 4-node tetrahedral elements (137,000 DOF) to 1,409,000 nodes and 1,038,000 10-node tetrahedral elements (4,200,000 DOF). As expected, more refined meshes resulted in better solutions, i.e. closer to that obtained on the original virtual eye, as observed in the predicted vitreo-retinal interface deformations and maximum principal strain fields at IOP $= 50$ mmHg. For a given nodal density 10-node tetrahedrals produced more accurate solutions than 4-node tetrahedrals. However, the differences between solutions computed for any two virtual eye reconstruction models were very small, with mean difference in displacement under 2 μm (standard deviation under 5 μm) and 0% mean difference in maximum principal strain (standard deviation under 1%).

Figure 7 shows computed maximum principal strain field in the original virtual eye model and a reconstructed model with a comparable number of nodes and elements. Also shown is the computed anterior-posterior deformation field zeroed on the vitreo-retinal interface at 5° from the axis of symmetry, consistent with a 10° field-of-view HRT acquisition. Within 10° of the axis of symmetry both models were formed by approximately 670,000 nodes and 470,000 10-node tetrahedrals (2,000,000 DOF). Excellent agreement in the vitreo-retinal interface deformations is evident (difference mean is 2 μm with a standard deviation of 3 μm). In particular, even though axisymmetry was not forced during the reconstruction or modeling steps, the reconstructed model shows a high degree of axisymmetry. The agreement in the maximum principal strains is also very good (difference mean is 0%, with a standard deviation under 1%), although less so than for deformations. This slightly poorer agreement is due to the fact that strain is obtained by differentiation of deformations, so that small differences in predicted deformations are accentuated. Nonetheless, strain patterns are very similar between the two models, and for purposes of predicting how cells will respond to mechanical loading, are for all practical purposes identical

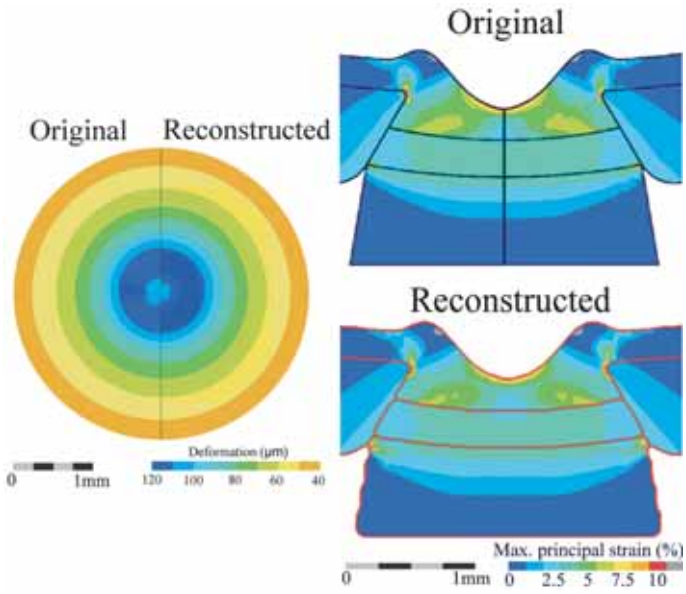

Fig. 7. Comparison between computed deformations and strains in the original and reconstructed virtual eye models. Left panel is an en face view of the deformations of the vitreo-retinal interface between IOPs of 5 and 50 mmHg. Deformations are zeroed at 5° from the centre of the optic cup. Right panel shows maximum principal strain contour levels at IOP = 50 mmHg with region boundaries outlined. Ideally both models would produce identical results. Both models were formed by 10-node tetrahedra and had approximately two million degrees of freedom within 10° of the axis of symmetry. In addition the original model had half a million degrees of freedom for the rest of the ocular shell.

3.2. Reconstructing individual-specific human ONHs

An individual-specific ONH model was constructed from the right eye of a 91 year old male enucleated 10 hours post mortem, imaged 15 hours later and fixed at 5 mmHg. The reconstructed ONH region is shown in Fig. 8.

A second individual-specific ONH model, including major blood vessels, was constructed from the right eye of a 79 year old male enucleated 2 hours post mortem and imaged with scanning laser tomography 21.5 hours later. The HRT reflectivity image of its optic disk is shown in Fig. 9, along with a superposed blood vascular tree. Note the good match in vascular tree geometry, particularly in the central region. The rms distance between the reconstructed vitreo-retinal interface and the HRT-measured topography at an IOP of 5 mmHg was 32.29 μm.

3.3. Mesh-independence study for individual-specific ONH model

The model shown in Fig. 9 was used for a mesh independence study, as well as for a comparison between experimentally measured and numerically predicted deformations of the vitreo-retinal interface as IOP was changed from 5 to 50 mmHg (Fig. 10). A series of four models, A to D, with varying nodal densities were used. Model A was the coarsest with approximately 135,000 nodes (90,000 elements and 400,000 DOF). Model B had 246,000 nodes (172,000 elements and 730,000 DOF). Model C had 532,000 nodes (377,000 elements and 1,229,600 DOF). Model D was the most refined with 938,000 nodes (670,000 elements and 2,765,000 DOF).

The deformations computed on all models were of the same order of magnitude as the measured deformation, and had a similar “kidney-shaped” profile (red zones of the middle column, Fig. 10). This

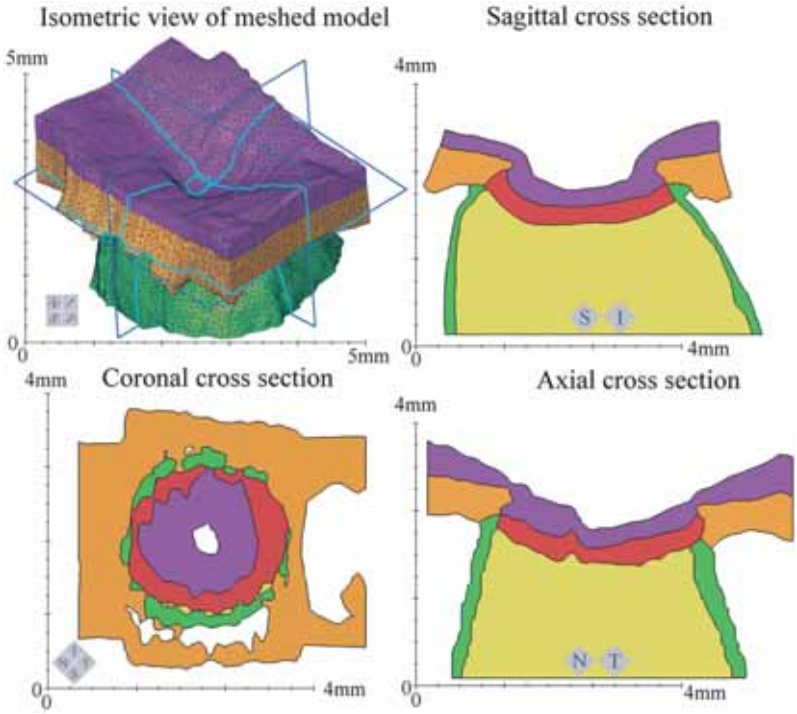

Fig. 8. A reconstructed individual-specific model of a human optic nerve head. Top left panel shows an isometric exterior view of the complete meshed model. The three other panels show Sagittal (Superior/Inferior), axial (Nasal/Temporal) and coronal cross sections through the model. The intersections between the planes of these sections (dark blue) and the full model are shown in the isometric view (light blue). Tissues are differentiated by color: purple- pre-laminar neural tissue, including the retina; orange – sclera: green – pia mater; yellow – post-laminar neural tissue (optic nerve); and red – lamina cribrosa. Legend: S = Superior; I = Inferior; N = Nasal; T = Temporal.

agreement between computed and measured deformations is encouraging and suggests that the modeling procedure described here is producing reasonable results. Mesh refinement had a small but noticeable effect in the predicted maximum principal strain field, but this was not mirrored by the predicted vitreo-retinal interface deformation. This is more easily seen in the computed change in deformation from one model to another (shown in absolute value in the right column of Fig. 10). As nodal density increased, the mean difference between models' predicted deformations diminished from 0.66 μm to 0.38 μm (standard deviations of 0.61 μm and 0.21 μm respectively), converging to a distribution very close to that predicted by the coarsest model.

To validate the way in which boundary conditions were applied to the patient-specific model, as described in Section 2.8, we computed the total force acting on the "edge" surface of a rectangular region 2.64 by 3.33 mm centered at the axis of symmetry for both the generic and the individual-specific models of Figs 9 and 10. The total force vectors differed by less than 0.4% in magnitude and by less than 3 $^\circ$ in alignment, suggesting that the deformation bounadary conditions computed in the generic shell could be applied to the individual-specific models.

3.4. Equilibration study (*viscoelastic effects*)

Typical data from an equilibration experiment are shown in Fig. 11, where an eye maintained at 14.3 mmHg IOP for an extended period was suddenly subjected to an IOP of 28.6 mmHg. The first

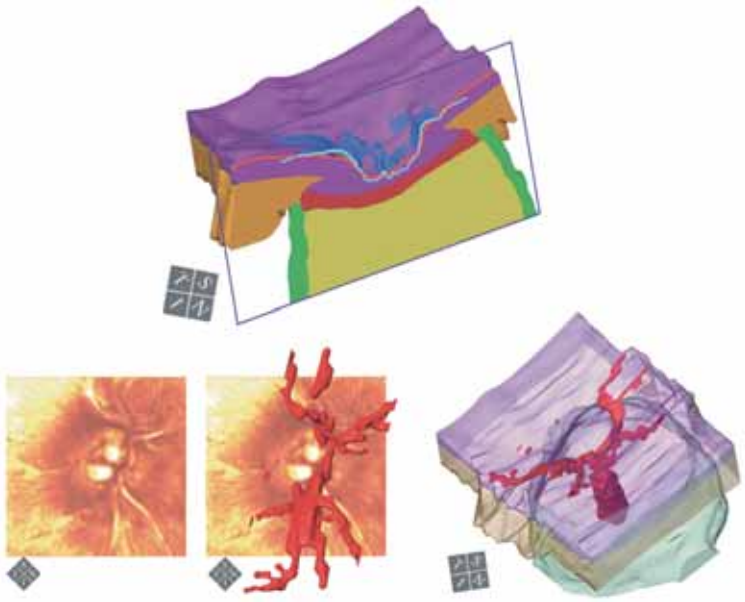

Fig. 9. Top panel shows a cut through a reconstructed individual-specific ONH, with the vitreo-retinal interface registered to the HRT-measured topography of the optic disk at 5 mmHg (dark blue). The two thin lines are the intersections of the cut plane and the reconstructed (red) and HRT-measured (light blue) surfaces. The reflectivity image is shown on the bottom left, with major retinal blood vessels reconstructed from the histological sections superposed in the middle panel. The bottom right panel shows a semi-transparent view of the ONH model with the vascular tree in red. Legend: S = Superior; I = Inferior; N = Nasal; T = Temporal.

scan after the pressure elevation (central panel) shows a large difference in retinal surface topography. These differences decreased with time, with the difference between 5 and 15 minutes after pressure elevation being much smaller (right panel). Subsequent measurements (i.e. for longer than 15 minutes after pressure elevation) showed minimal change. We therefore set the equilibration interval, i.e. the time between a change in IOP and scanning the vitreo-retinal interface topography, to fifteen minutes.

4. Discussion and conclusions

The goal of this paper was to introduce methodology for producing individual-specific models of the human optic nerve head, to validate the methodology, and to give examples of its use. A second goal was to determine the experimental conditions that would allow the elastic (as opposed to the viscoelastic) response of the optic nerve head to be measured.

4.1. Individual-specific ONH models

The construction process described herein is clearly capable of producing ONH models whose biomechanics can be analyzed using finite element methods. To our knowledge the procedures described here are the first reported that allow individual-specific reconstruction of a complete human ONH. Similar techniques have been reported for monkey optic nerve heads [15,30,31]. The central question then becomes one of fidelity: how well does the reconstructed model mimic the actual biomechanics of the optic nerve head? We cannot know this with certainty, since there is no “gold standard” method for

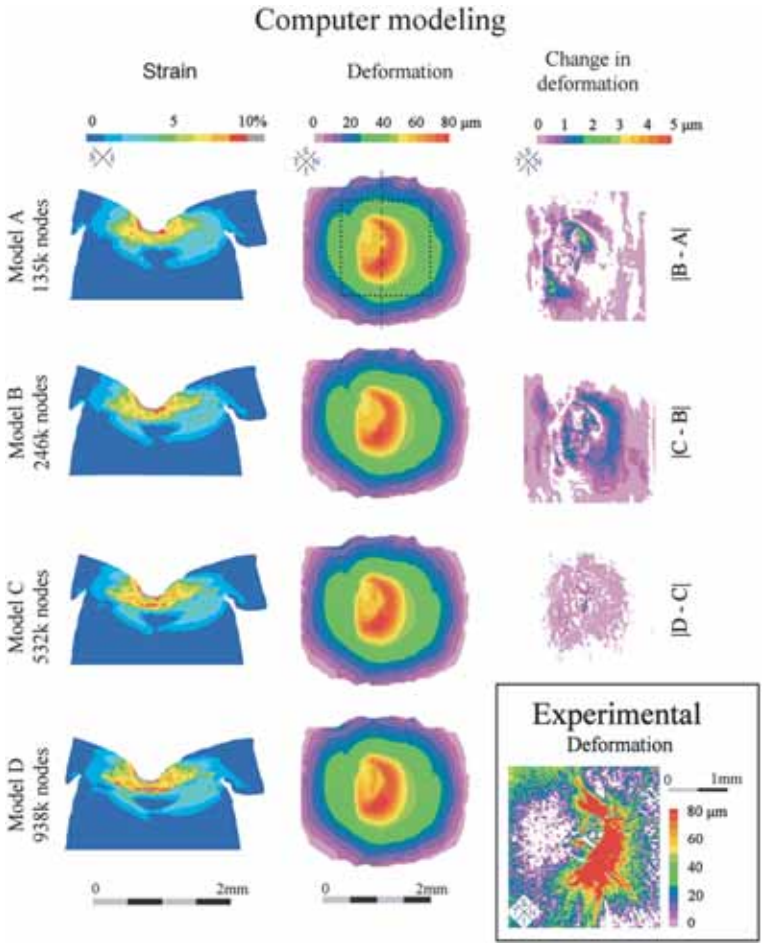

Fig. 10. Comparison between experimentally measured and numerically computed IOP-induced deformations for the individual-specific ONH model shown in Fig. 9. Four different models with various nodal densities were produced (see labels at left) and the resulting deformation and principal strain fields were compared. The left column shows sagittal cross sections through the center of the cup with colours corresponding to contour levels of predicted maximum principal strain at an elevated IOP of 50 mmHg. Middle column shows the predicted vitreo-retinal interface deformation when IOP increases from 5 to 50 mmHg. Right column shows the change in deformation predicted by the different models in the central region (shown by the dotted square in the coarsest model deformation). The dotted vertical line in the coarsest model deformation represents the sagittal plane through which the strain sections are shown. The inset in the bottom right is the experimentally measured deformation of the vitreo-retinal interface, which should be compared with the dotted square region of the panels in the middle column. All deformations are zeroed at 5° from the centre of the optic cup. The HRT deformations were computed using the HRT's own glaucoma progression analysis routines.

determining optic nerve head anatomy against which we can compare our reconstructions. This question is not an abstract one: when reconstructing tissues from serial sections there are unfortunately several possible sources of geometric inaccuracy. These include potential tissue deformation during preparation, histologic section deformation during sectioning, staining and mounting, mis-alignment of digitized sections, and the reconstruction process itself. We therefore turned to the use of a "virtual eye" to help assess the suitability of our reconstruction process.

Our reconstruction of a virtual eye suggests that the construction and finite element modeling methods presented here are suitable. More specifically, although there were small differences in the computed

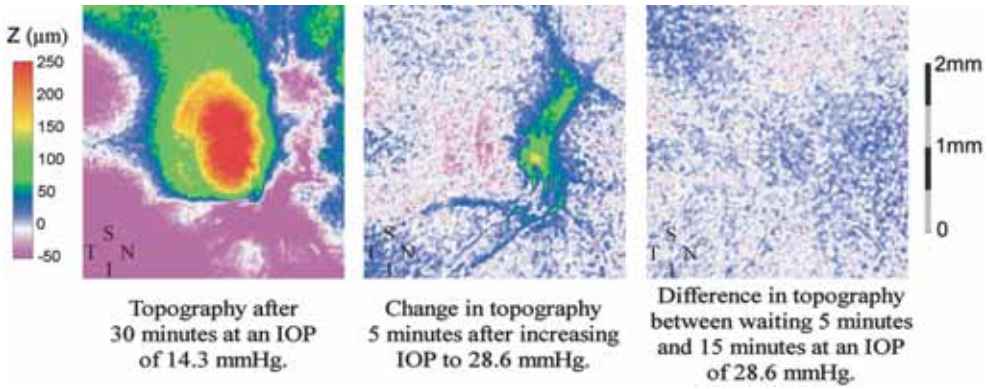

Fig. 11. Typical experimental results obtained with the scanning laser tomographer (HRT) in the equilibration tests. The left panel shows the vitreo-retinal interface topography at an IOP of 14.3 mmHg, a normal level. The central panel shows the change in topography produced by a step increase of IOP to an elevated 28.6 mmHg, taken 5 minutes after the increase. Sinking (posterior displacement) of the cup is visible, mostly on the nasal (N) side. A further wait of 10 minutes has a much smaller effect, as can be seen on the right panel, showing the difference in topography between 5 and 15 minutes at an elevated 28.6 mmHg. Differences were computed using the HRT's glaucoma progression analysis routines.

strain fields for the reconstructed geometry when compared to the true geometry, they were not significant enough to change our understanding of the biomechanics of the optic nerve head. This result is encouraging, and strongly suggest that the approach that we have adopted gives a good representation of optic nerve head biomechanics. Some caution should be exercised in extrapolating this conclusion to real tissue, since there are differences between virtual sections and real histological sections: virtual sections are perfectly aligned and equally spaced, have no deformation and all tissue boundaries are unequivocal. This means that we should think of the reconstruction process on the virtual eye as a "best-case" scenario.

Further confidence in the reconstruction process is provided by the relatively good match in blood vessels geometry between the HRT reflectivity image and the reconstructed model, and the good registration between the HRT-measured optic disk topography and the reconstructed vitreo-retinal interface (Fig. 10). Also, the measured and computed vitreo-retinal interface deformations in the individual-specific model show a remarkably similar overall deformation pattern. The largest discrepancy between measured and computed deformations are the steep deformation gradients seen experimentally that are not present in computations. The source(s) of this difference is still unclear, but may be related to errors in the assumed constitutive relationships for the ONH tissues. In addition, the mechanical response to IOP was predicted on an ONH that did not include blood vessels, which can collapse at elevated IOP and may be important in ONH biomechanics, at least in the *ex vivo* situation evaluated here. A larger study that reconstructs optic nerve heads of eyes from a wider sample is already under way.

The ONH reconstruction process has several limitations. For example, the process is destructive, requiring sectioning of the optic nerve head. Further, certain steps in the process are subjective. Notably, the complexity of the geometry, the limited information available in 2D serial sections and inhomogeneous staining make segmentation subjective. However, given the limits of our capabilities to model the biomechanics of the ONH tissues, such as uncertainty about material properties, we believe that the methodology described is a reasonable approach that provides a good balance between accuracy and simplicity. Resolving the ONH in much higher resolution would be desirable from some perspectives, but it would increase the difficulty of modeling the whole region, and the number and type of tissues that can be considered. Less resolved models run the risk of missing essential geometric information. However, we acknowledge that our current method is incapable of reproducing some details of the ONH

that could possibly be related to glaucoma, for example, snapping of laminar beams and/or axoplasmic flow.

The models constructed with the method described here are the foundation for future finite element analysis of ONH biomechanics based on individual-specific geometries. They describe the entire optic nerve head region in detail, and allow realistic boundary conditions to be applied to individual-specific ONH models. Such models will allow us to accurately simulate human optic nerve head biomechanics and its relation with glaucomatous vision loss.

4.2. Viscoelastic tissue response

Experimental data shows that an equilibration time of 15 minutes at each pressure is sufficient to obtain a stable deformation of the vitreo-retinal interface. This suggests that characteristic time scales for viscoelastic effects are shorter than 15 minutes for ONH tissues. Because we carried out all imaging studies after a 15 minute wait time at each IOP level, this implies that our retinal topography imaging was measuring the elastic, rather than viscoelastic, response of the tissue.

Acknowledgements

This work was supported by the Consejo Nacional de Ciencia y Tecnología de México (IAS) and by the Canadian Institutes for Health Research (CRE, JGF), and Glaucoma Research Society of Canada. We thank the Eye Bank of Canada for providing donor tissue.

References

[1] H.A. Quigley, Number of people with glaucoma worldwide, *Br J Ophthalmol* **80** (5) (1996), 389–393.
[2] H.A. Quigley, R.W. Flower, E.M. Addicks and D.S. McLeod, The mechanism of optic nerve damage in experimental acute intraocular pressure elevation, *Invest Ophthalmol Vis Sci* **19**(5) (1980), 505–517.
[3] H.C. Geijssen, *Studies on Normal Pressure Glaucoma*, Kugler Publications, 1991.
[4] AGIS I, The advanced glaucoma intervention study (Agis): 7. The relationship between control of intraocular pressure and visual field deterioration. The Agis Investigators, *Am J Ophthalmol* **130**(4) (2000), 429–440.
[5] M.C. Leske, A. Heijl, M. Hussein, B. Bengtsson, L. Hyman and E. Komaroff, Factors for glaucoma progression and the effect of treatment: The early manifest glaucoma trial, *Arch Ophthalmol* **121**(1) (2003), 48–56.
[6] M.C. Leskea, A. Heijl, L. Hyman, B. Bengtsson and E. Komaroff, Factors for progression and glaucoma treatment: The early manifest glaucoma trial, *Curr Opin Ophthalmol* **15**(2) (2004), 102–106.
[7] J.C. Downs, J.K. Suh, K.A. Thomas, A.J. Bellezza, C.F. Burgoyne and R.T. Hart, Viscoelastic characterization of peripapillary sclera: Material properties by quadrant in rabbit and monkey eyes, *J Biomech Eng* **125**(1) (2003), 124–131.
[8] M.R. Hernandez, The optic nerve head in glaucoma: Role of astrocytes in tissue remodeling, *Prog Retin Eye Res* **19**(3) (2000), 297–321.
[9] E.F. Ellis, J.S. McKinney, K.A. Willoughby, S. Liang and J.T. Povlishock, A new model for rapid stretch-induced injury of cells in culture: Characterization of the model using astrocytes, *J Neurotrauma* **12**(3) (1995), 325–339.
[10] D.B. Yan, J.G. Flanagan, T. Farra, G.E. Trope and C.R. Ethier, Study of regional deformation of the optic nerve head using scanning laser tomography, *Curr Eye Res* **17**(9) (1998), 903–916.
[11] N.S. Levy and E.E. Crapps, Displacement of optic nerve head in response to short-term intraocular pressure elevation in human eyes, *Arch Ophthalmol* **102**(5) (1984), 782–786.
[12] M.E. Edwards and T.A. Good, Use of a mathematical model to estimate stress and strain during elevated pressure induced lamina cribrosa deformation, *Curr Eye Res* **23**(3) (2001), 215–225.
[13] H. Dongqi and R. Zeqin, A biomathematical model for pressure-dependent lamina cribrosa behavior, *J Biomech* **32**(6) (1999), 579–584.
[14] S. Bauer and E. Voronkova, *Mechanical Aspects of the Development of the Glaucomatous Atrophy of the Optic Nerve Fibres*, Ocular Biomechanics Conference, Moscow, 2001, Helmholtz Research Institute for Eye Diseases.

[15] A.J. Bellezza, R.T. Hart and C.F. Burgoyne, The optic nerve head as a biomechanical structure: Initial finite element modeling, *Invest Ophthalmol Vis Sci* **41**(10) (2000), 2991–3000.
[16] I.A. Sigal, J.G. Flanagan, I. Tertinegg and C.R. Ethier, Finite element modeling of optic nerve head biomechanics, *Invest Ophthalmol Vis Sci* **45**(12), 4378–4387.
[17] C.R. Ethier, I. Tertinegg, D.B. Yan, G.E. Trope and J.G. Flanagan, *A System for Studying Lamina Cribrosa Biomechanics in Human Eyes*, 1st Joint Meeting BMES & EMBS, 1999, pp. 1312–1313.
[18] G.E. Trope, J.G. Flanagan, I. Tertinegg and C.R. Ethier, A new method for studying lamina cribrosa behavior in human eyes, *Invest Ophthalmol Vis Sci* **41**(Suppl 4) (2000), 950.
[19] A.J. Bellezza, *Biomechanical Properties of the Normal and Early Glaucomatous Optic Nerve Head: An Experimental and Computational Study Using the Monkey Model*, Doctoral thesis, Department of Biomedical Engineering, Tulane University, 2002.
[20] J. Hecksher-Sorensen and J. Sharpe, 3d Confocal reconstruction of gene expression in mouse, *Mech Dev* **100**(1) (2001), 59–63.
[21] H.A. Quigley and E.M. Addicks, Regional differences in the structure of the lamina cribrosa and their relation to glaucomatous optic nerve damage, *Arch Ophthalmol* **99**(1) (1981), 137–143.
[22] J.B. Jonas and W.M. Budde, Diagnosis and pathogenesis of glaucomatous optic neuropathy: Morphological aspects, *Prog Retin Eye Res* **19**(1) (2000), 1–40.
[23] R. Enciso, A. Memon and J. Mah, Three-dimensional visualization of the craniofacial patient: Volume segmentation, data integration and animation, *Orthod Craniofacial Res* **6**(Suppl. 1) (2003), 66–71.
[24] H.-C. Hege, M. Seebass, D. Stalling and M. Zöckler, A Generalized Marching Cubes Algorithm Based on Non-Binary Classifications, Technical report SC-97-05, Zuse-Institute-Berlin (ZIB), 1997,
[25] M. Westerhoff, *Efficient Visualization and Reconstruction of 3d Geometric Models from Neuro-Biological Confocal Microscope Scans*, Doctoral thesis, Department of scientific visualization of the Zuse Institute Berlin (ZIB), Freie Universitat Berlin, Berlin, 2003.
[26] Amira, User's Guide and Reference Manual V3.1, TGS Template Graphics Software Inc USA.
[27] E. Gladilin, *Biomechanical Modeling of Soft Tissue and Facial Expressions for Craniofacial Surgery Planning*, Doctoral thesis, Free University of Berlin, Berlin, 2003.
[28] ANSYS, ANSYS V6.1 Online Reference Manual, Theory Reference, Section 19.7., 2001.
[29] R.D. Cook, *Finite Element Modeling for Stress Analysis*, John Wiley & Sons, Inc., 1995.
[30] R.C. Anderson, C.F. Burgoyne, A.J. Bellezza, J.C. Downs and R.T. Hart, *Finite Element Modeling of Anterior Laminar Disinsertion in Early Experimental Glaucoma*, (Vol. 45), E-Abstract 2155, Ft. Lauderdale, FL, USA: ARVO; 2004.
[31] J.C. Downs, R.T. Hart, V. Grau, A.J. Bellezza, B.A. Hirons and C.F. Burgoyne, *Micro Finite Element Modeling of the Lamina Cribrosa in Monkey Eyes*, (Vol. 45), E-Abstract 2157, Ft. Lauderdale, FL, USA: ARVO; 2004.
[32] I. Fatt and B.A. Weissman, *Physiology of the Eye: An Introduction to the Vegetative Functions*, (2nd ed.), Butterworth-Heinemann, 1992.